

Tuning the intrinsic anomalous Hall effect from large to zero in the two ferromagnetic states of the layered SmMn_2Ge_2

Mahima Singh, Jyotirmoy Sau, Banik Rai, Arunanshu Panda, Manoranjan Kumar[#],

Nitesh Kumar*

S. N. Bose National Centre for Basic Sciences, Salt Lake City, Kolkata-700106, India

[#manoranjan.kumar@bose.res.in](mailto:manoranjan.kumar@bose.res.in)

[*nitesh.kumar@bose.res.in](mailto:nitesh.kumar@bose.res.in)

Abstract

The intrinsic anomalous Hall conductivity in a ferromagnetic metal is completely determined by its band structure. Since the spin orientation direction is an important band structure tuning parameter, it is highly desirable to study the anomalous Hall effect in a system with multiple spin reorientation transitions. We study a layered tetragonal room temperature ferromagnet SmMn_2Ge_2 , which gives us the opportunity to measure magneto-transport properties where the long c -axis and the short a -axis can both be magnetically easy axes depending on the temperature range we choose. We show a moderately large completely intrinsic anomalous Hall conductivity (AHC) up to room temperature when the crystal is magnetized along c -axis. Interestingly, the AHC can be tuned to completely extrinsic with extremely large values when the crystal is magnetized along a -axis irrespective of whether the a -axis is magnetically easy or hard axis. The first principles calculations show that nodal line states originate from Mn- d orbitals just below the Fermi energy (E_F) in the electronic band structure when the spins are oriented along the c -axis. Intrinsic AHC originates from the Berry curvature effect of the gapped nodal lines in the presence of spin-orbit coupling. AHC almost vanishes when the spins are aligned along the a -axis because nodal line states shift above E_F and become unoccupied states.

Introduction

Topology in time reversal symmetry broken systems has been a subject of intense research recently. Berry curvature effects which are at the centre of these topological materials can manifest itself at momentum space or real space to impart exotic transport characteristics.¹⁻³ Berry curvature-induced anomalous Hall effect is one such avenue which has engaged solid state physicists and materials scientists lately.^{4,5} Attributes in the crystal structure such as kagome and square-net sub-units have additionally attracted the focus towards layered ferromagnets apart from obvious van der Waals ferromagnets.⁵⁻⁸ One important feature of these layered ferromagnets is that they contain strong uniaxial magnetic anisotropy. Many recent studies signify intrinsic anisotropic anomalous Hall conductivity in layered ferromagnets when the magnetic field is applied along the magnetic easy axis. Often, it is not possible to access different crystallographic axes as easy axes of magnetization in a structurally anisotropic compound without structural phase transition. For example, the long crystallographic c -axis remains the easy magnetization axis for many hexagonal and tetragonal systems. Hence, it is highly desirable to investigate systems where one can have the freedom to study AHE by tuning the magnetic easy axis from one crystallographic direction to another.

We choose SmMn_2Ge_2 to study anisotropic magneto-transport property since it is known to exist in at least three magnetically ordered states with spontaneous alignment of spins along in-plane and out of the plane directions. Among RMn_2Ge_2 family of compounds, the magnetic states are known to be dictated by the intra-layer nearest Mn-Mn distance ' d ' within the square nets of Mn. From the literature it is known that $d < 2.87\text{\AA}$ promotes antiferromagnetic ordering while $d > 2.87\text{\AA}$ favours ferromagnetic ordering.⁹ SmMn_2Ge_2 stands out to its proximity to the critical value of d . Temperature is the obvious parameter that can smoothly change d across the critical value. Indeed, temperature results in multiple magnetic phase transitions and re-entrant ferromagnetism. SmMn_2Ge_2 attains ferromagnetism at $T_C \sim 350$ K. As the temperature

decreases from T_C , the ferromagnetic (FM) phase undergoes a sharp transition into an antiferromagnetic (AFM) phase around 150 K. This is because the thermal contraction causes d to decrease, ultimately dropping below the critical value of 2.87\AA .^{10,11} In the AFM state, it is suggested that the interaction between Sm and Mn atoms weakens compared to the coupling between Mn-Mn atoms. However, as the temperature goes below 100 K, the Sm-Sm coupling becomes intense and is sufficient to break AFM Mn-Mn coupling, resulting in the emergence of the re-entrant ferromagnetic (RFM) phase in the system.⁹

LaMn_2Ge_2 and NdMn_2Ge_2 which are sister compounds to SmMn_2Ge_2 have recently gathered attention due to the occurrence of large topological Hall effect.^{12,13} In this work, we have investigated the correlation between transport and magnetic properties such as the presence of AHE with re-entrant ferromagnetism. The systematic magnetic and electrical transport measurements have been performed with respect to the field along different crystallographic directions. By changing magnetic field direction, $H\parallel c$ to $H\parallel ab$, AHE interestingly changes from completely intrinsic to completely extrinsic.

Method

High-quality single crystals of SmMn_2Ge_2 were prepared by flux method using Indium (In) flux. Pieces of the elements were mixed in the stoichiometric ratio of Sm:Mn:Ge:In = 1:2:2:60 and were put into an alumina crucible which was sealed under vacuum. The sealed quartz tube was placed inside the furnace, slowly heated up to 1050°C , and dwelt for 24 h. Afterwards, it was slowly cooled down to 700°C at the rate 2°C/h . To separate single crystals from In flux, the tube was taken out at 700°C and centrifuged. Plate-like single crystals were obtained. The crystal structure of prepared single crystals was characterized using an X-ray diffractometer (XRD, smart lab, Rigaku) equipped with Cu- K_α radiation. To verify the Chemical composition

of samples, we have performed Energy dispersive X-ray spectroscopy (EDX). The magnetic measurements were performed by using a Vibrating sample magnetometer (VSM) on a physical properties measurement system (PPMS, Dynacool, Quantum Design). The electrical transport measurements under magnetic field were carried out using electrical transport option (ETO) of PPMS. A rectangular-shaped crystal of the size of 1.2mm×0.59mm×0.54mm was used for magneto-transport and magnetic measurements. A standard four probe method was used to perform longitudinal and Hall resistivity measurements. To cancel out the longitudinal resistivity contribution due to probe misalignment, the Hall resistivity was antisymmetrized using the relation $\rho_H(H) = \frac{\rho_H(+H) - \rho_H(-H)}{2}$.

Ab initio calculations of the electronic structure of SmMn₂Ge₂ were performed using density functional theory (DFT) with the generalised gradient approximation (GGA) of the exchange correlation functional¹⁴ implemented in the Vienna ab initio simulation package code¹⁵. The effective Coulomb exchange interaction $U_{eff} (U-J)$, where U and J are the Coulomb and spin exchange parameters, is used to incorporate the strong on-site Coulomb repulsion, also called Hubbard $U_{eff} = 3.0$ eV for the d-orbitals of the Mn atoms. For this value of U , the calculated value of the average magnetic moment, is in agreement with the experiment. The cut-off energy for the expansion of the wave functions into the plane wave basis was kept constant throughout at 600 eV. The Brillouin zone was sampled in the k-space of the Monkhorst-Pack scheme for the calculation. The equilibrium structure served as the basis for the K-grid, which was 10×10×6. In the next step, Wannier functions were extracted from the DFT band structure via the WANNIER90 package.^{16,17} A tight-binding Hamiltonian was constructed from the Wannier functions to calculate the Berry curvature via the Kubo formula using Wanniertools.¹⁸ The intrinsic Hall conductivity (σ_{xy}^{int}) is calculated by integrating the z -component of the Berry

curvature (Ω_z) over all occupied states throughout the Brillouin zone, considering the spin-orbit coupling.

Results

SmMn_2Ge_2 crystals grow in a tetragonal ThCr_2Si_2 -type crystalline structure with space group $I4/mmm$ [19]. Within this structure, all Sm, Mn and Ge atoms are stacked in layers along c-axis occupying 2a (0,0,0), 4d (0,0.5,0.25) and 4e(0,0,z) Wyckoff positions, respectively as shown in Fig. 1(a). Mn atoms form a square net structure along ab -plane which is depicted by a yellow plane for a guide to eye. An optical image of a typical crystal is presented in the inset of Fig. 1(b). The composition of the crystals is very close to SmMn_2Ge_2 (see Fig. S1(a)). The XRD pattern (see Fig. 1(b)) obtained on a crystal by keeping the flat plane along the sample holder reveals reflections corresponding only to $(00l)$ planes, confirming the exposed plane to be the ab -plane. To confirm the single crystalline nature of the sample we performed Laue X-ray diffraction by exposing the-ray perpendicular to the flat plane. The diffraction pattern consists of four-fold symmetric points which is consistent with the tetragonal structure with $I4/mmm$ space group. Sharp spots in the pattern indicate good quality of the single crystal. The diffraction pattern fits well with space group $I4/mmm$ using reported cell parameters (see Fig. S1(b)).

Fig. 1 (d) shows the magnetization (M) vs temperature (T) data obtained by applying a magnetic field of 200 Oe along the c-axis. As mentioned earlier, upon decreasing temperature, the paramagnetic SmMn_2Ge_2 becomes ferromagnetic at ~ 340 K where the moment on Mn and Sm layers points out of the layer (along c-axis). We call this FM phase as FM-1. As the temperature is decreased, an antiferromagnetic (AFM) phase is achieved at ~ 140 K, which can be inferred from the vanishing net magnetic moment. The AFM persists up to ~ 100 K below which it attains a re-entrant FM phase which we call FM-2 phase. FM-2 phase is stable up to the lowest

measurement temperature of 2 K. The spins on Mn and Sm orient themselves ferromagnetically in the ab-plane. This is also evident from the seven-times smaller net magnetization of FM-2 phase compared to that in the FM-1 phase. We have shown the M vs T data when the magnetic field of 200 Oe is applied in the ab-plane along [100] (see Fig. S2). All the features are same except that the FM-2 phase has much higher magnetisation than FM-1 phase. The important observation here is that in FM-1 phase, c-axis is the easy axis of magnetization which changes to easy ab-plane of magnetization in the FM-2 phase. Longitudinal resistivity (ρ_{xx}) as a function of temperature while applying the current along a-axis decreases as the temperature is decreased, verifying the metallic nature of the material. The slope of the ρ_{xx} vs T data changes at the paramagnetic to FM-1 phase and we also observe small kinks corresponding to the FM-1 to AFM and AFM to FM-2 phase transition, which are consistent with previous reports. The resistivity at 300 K and 2 K are 228 $\mu\Omega$ -cm and 1.55 $\mu\Omega$ -cm which accounts for a large residual resistivity ratio ($RRR = \frac{\rho_{xx}^{300K}}{\rho_{xx}^{2K}}$) of 147. For some other crystals (see Fig. S3) we found even larger RRR of 278 demonstrating excellent quality of the grown crystals.

In Fig. 2(a) we show $M - \mu_0 H$ data while applying the magnetic field along c-axis for temperatures at 300 K, 125 K and 2 K representing the FM-1, AFM and FM-2 phase, respectively. In FM-1 phase (300 K) magnetization saturates at a small field of 0.16 T in accordance with the spontaneous alignment of spins along c-axis. The saturation magnetization (M_S) is $\sim 2 \mu_B/\text{f.u.}$ In the FM-2 (2 K) phase the magnetization continuously increases and does not saturate up to 5 T because c-axis is the hard axis in this phase. In the AFM (125 K) phase we observe a spin flop transition at 1 T where there is sudden increase of magnetization followed by a slow saturation of magnetization at ~ 1.75 T to value of $\sim 3.1 \mu_B/\text{f.u.}$ When the magnetic field is applied along [100] as shown in Fig. 2(b), in FM-1 phase (300 K) the magnetization is difficult to saturate (3 T, to a value of $\sim 2 \mu_B/\text{f.u.}$) compared to the FM-2 phase

(2 K) where it easily saturates to a value of $\sim 3.7 \mu_B/\text{f.u.}$ at a small magnetic field of 0.4 T. In the AFM phase (125 K) we observe a spin-flip transition at ~ 0.4 T which corresponds to a sharp saturation of magnetization. These observations are at good agreement with the previous reports.⁹ $M - \mu_0 H$ data at other temperatures with magnetic field along [001] and [100] are shown in Fig. S4.

To investigate the effect of magnetic anisotropy on the electrical transport behavior of SmMn_2Ge_2 in different crystallographic directions, we performed measurements of ρ_{xx} and ρ_{yx} . Fig. 3(a) shows the Hall resistivity (ρ_{yx}) when the current is flowing along the a-axis and the magnetic field is applied along the c-axis at temperatures belonging to the FM-1 phase. In metallic systems with spontaneous magnetization the total Hall resistivity can be expressed as $\rho_{yx} = \rho_{yx}^N + \rho_{yx}^A = R_0 B + R_S M_S$ where, ρ_{yx}^N is the normal Hall resistivity component, ρ_{yx}^A is the anomalous Hall resistivity component, R_0 is the normal Hall coefficient, R_S is the anomalous Hall coefficient and M_S is the saturation magnetization. At 300 K, ρ_{yx} increases rapidly before saturating at ~ 0.16 T and then changes very slowly with field. The behavior of ρ_{yx} mimics that of M , suggesting the presence of an anomalous Hall effect (AHE). The value of the anomalous Hall resistivity (ρ_{yx}^A) is estimated by fitting the normal Hall region by a linear function and extending it to zero field to find out ρ_{yx}^A as the intercept on y-axis. Hall conductivity σ_{xy} is calculated from the tensor relation $\sigma_{xy} = \frac{\rho_{yx}}{\rho_{yx}^2 + \rho_{xx}^2}$. The same protocol as ρ_{yx}^A is used to estimate the value of σ_{xy}^A from the magnetic field-dependent data of σ_{xy} . σ_{xy}^A has been known to arise mainly through three main mechanisms namely, intrinsic Karplus-Luttinger mechanism, and extrinsic skew scattering and side jump mechanism.² Since, the intrinsic contribution to σ_{xy}^A is entirely electronic Berry curvature-dependent and does not depend on the scattering effects, one expects it to be temperature independent. Fig. 3(b) shows temperature dependence of σ_{xy}^A as a function of temperature in FM-1 phase. It has a feeble

dependence on temperature with lowest and highest values being $\sim 105 \Omega^{-1}\text{cm}^{-1}$ and $77 \Omega^{-1}\text{cm}^{-1}$, respectively which accounts for approximately 25 % decrease. However, a scattering-dependent quantity i.e. σ_{xx} has a large dependence on temperature with values at 150 K and 300 K being $11.1 \times 10^4 \Omega^{-1}\text{cm}^{-1}$ and $3.8 \times 10^4 \Omega^{-1}\text{cm}^{-1}$, respectively (see Fig 3(b)). A small decrease in σ_{xy}^A mentioned above can also be accounted for if one investigates the variation of saturation magnetization in same temperature range. This has been shown in Fig. S5 where we observe a change in magnetization of approximately 25 %. This means that σ_{xy}^A effectively does not at all vary pointing towards the intrinsic origin of AHE. This claim is further confirmed by analyzing the scaling behavior, where we plot ρ_{yx}^A / M_S with respect to ρ_{xx}^2 which results in a perfect straight line.¹⁹ This scaling law in other words suggest the same point that the anomalous Hall conductivity corrected by a varying saturation magnetization is a constant and hence does not depend on scattering time. Although, the ab-plane is a hard magnetic plane in FM-1 temperature range, $M - \mu_0 H$ curves still saturate around 2 T magnetic field along a-axis. We expect, the same behaviour in the corresponding Hall resistivity data when the magnetic field is applied along [010]. Fig. 3(d) shows Hall resistivity (ρ_{zx}) as a function of magnetic field where the current and magnetic field are applied along crystallographic *a*- and *c*-axis, respectively. Like magnetization saturation, $\rho_{zx} - \mu_0 H$ data too saturate at ~ 2 T confirming the presence of finite AHE. Interestingly, the maximum value of σ_{xz}^A observed at 150 K is $456 \Omega^{-1}\text{cm}^{-1}$ which is much higher than σ_{xz}^A at the same temperature. However, the decrease in σ_{xz}^A with increasing temperature is much faster (see Fig. 3(e)) than that of σ_{xy}^A ; at 300 K, it could retain only 23 % ($105 \Omega^{-1}\text{cm}^{-1}$) of the maximum value. This hints towards an extrinsic behaviour of σ_{xz}^A . To confirm this, we plot ρ_{yx}^A / M_S against ρ_{xx} (see Fig. 3 (f)) which nicely fits with a straight line confirming that σ_{xz}^A is not temperature-independent and varies as a function of σ_{xx} (or scattering time). Hence, the AHE is dominated by extrinsic skew scattering

effect when the magnetic field is applied to magnetically hard crystallographic a -axis as compared to completely intrinsic effect when the magnetic field is along magnetically easy [001].

Now we turn our focus towards the FM-2 region where [100] or [010] is magnetically easy axis compared to the [001]. An important point to note here is that the [001] is very hard and does not show any signature of magnetic saturation in our magnetization measurements. Hence, for the magneto-transport studies, we only consider applying magnetic field along a -axis (easy-axis). To our surprise, we did not observe any AHE at 2 K although the magnetization saturates easily at a small magnetic field of 0.4 T. $\rho_{zx} - \mu_0 H$ data show a linear increase of ρ_{zx} with increasing magnetic field (see Fig. 3(g)) indicative of the normal Hall effect originating from hole-dominating carrier transport. We only start seeing the feature of AHE in $\rho_{zx} - \mu_0 H$ data at 50 K and above temperatures in this FM-2 region as shown in Fig. 3h. It is noteworthy that the corresponding σ_{xz}^A is extremely large with a value as large as $1400 \text{ } \Omega^{-1} \text{ cm}^{-1}$, however, this value decreases very rapidly with increasing temperature, again indicating that it originates from extrinsic origin (see Fig. S5). We perform the scaling analysis by plotting ρ_{yx}^A / M_S against ρ_{xx} and find a perfect straight line fit (see Fig. 3(i)) confirming that it originates from skew scattering mechanism.

In Fig. 4(a) we show $\rho_{yx} - \mu_0 H$ at different angles at 200 K (FM-1) with magnetic field along c -axis for $\theta = 0^\circ$ and along a -axis for $\theta = 90^\circ$. A hump-like feature can be observed in $\rho_{yx} - \mu_0 H$ data which are more pronounced at higher θ s. This feature is absent in the magnetisation data [shown for $\theta = 75^\circ$ in Fig. 4(b)], which at first sight suggests that the feature in $\rho_{yx} - \mu_0 H$ might be a topological Hall signal. However, we argue that this feature is just a consequence of the non-orthogonal Hall geometry and not a topological Hall signal. It is well known that if the magnetic field is not orthogonal to the current, then only the component of

the field perpendicular to the current (component along [001] in our case) will give rise to an ordinary Hall effect (OHE), and the component parallel to the current will not contribute to OHE. A similar argument applies to the anomalous Hall effect (AHE) also, where the role of the magnetic field is played by the magnetisation of the sample. The magnetisation shown in Fig. 4(b) is the net magnetisation of the sample for the given geometry and not just a component of it. To investigate how the magnetisation component along [001] (M_z) varies with the magnetic field, we refer to the domain theory of ferromagnetism. In a uniaxial ferromagnet, magnetic domains are typically aligned along the direction of the easy axis of magnetization ([001]). Initially, when no magnetic field is applied, there are two major domains of equal size (domain-A and domain-B in Fig. 4(c)) which are oppositely oriented parallel to [001] direction. To account for any other possible domains, we can consider two minor domains of equal size (domain-C and domain-D) which are oppositely directed and orthogonal to the major domains. However, the following argument is equally valid even if we do not consider domains-C and -D. When no magnetic field is applied, the moments in the oppositely directed domains cancel each other out, giving a zero net magnetisation [Fig. 4(c)]. When a magnetic field is applied at an angle θ away from [001] direction, the domains that are inclined towards the magnetic field (domains-A and -D) will expand, while the domains that are inclined away from the magnetic field (domains-B and -C) will shrink in size via domain wall motion. Because of the significant magnetocrystalline anisotropy of the sample, domain rotation is limited at lower fields. Domain wall motion continues until domains B and C nearly disappear, resulting in a sharp increase in both the net magnetization (M) and the [001] component of the net magnetization (M_z). As the field is further increased, the domains begin to rotate towards the magnetic field so that M continues to increase at a slower rate. Since the major magnetisation is contributed by domain-A and it rotates away from [001] with the increasing magnetic field, M_z begins to decrease. The domain rotation persists until all the domains are aligned with the magnetic field. M and M_z

reach a saturation value at this point, where M_z is given by the relation $M_z = M \cos\theta$. The typical shape of $M_z - \mu_0 H$ curve now looks like the shape of $\rho_{yx} - \mu_0 H$ curve. Thus, we conclude that the hump-like feature in $\rho_{yx} - \mu_0 H$ data has a magnetic origin and is not related to topological Hall effect. Since our argument is completely general to any anisotropic uniaxial ferromagnet, this hump-like feature in $\rho_{yx} - \mu_0 H$ data in non-orthogonal Hall geometry should be common in such systems which we really find in the literature.²⁰

The experimental result suggests that there is a change of easy magnetic axis with temperature across FM-1 and FM-2 phases due to the change in interatomic distances, hence we have carried out electronic structure calculations for these two phases. These calculations suggest that the minimum energy structures have a simple magnetic axis oriented along [001] at 300 K and along [100] at 0 K and these theoretical results agree with the experimental data. The dispersion of the energy bands at 300 K show linear crossings at the Fermi energy (E_F) along Γ -X and Γ -N. Most of these degeneracies at E_F are lifted in the presence of spin-orbit coupling (SOC) and form a nodal line. The red and blue lines represent the electronic band without and with SOC. The main contribution to the bands near E_F comes from the d -orbital of Mn. We have also calculated the z -component of Berry curvature (BC) along the high-symmetry path as shown in Fig. 5(b), and note distinct BC peaks along Γ -X and Γ -N. For further analysis of the class of degeneracies, the energy gap is calculated in the presence of SOC. SmMn_2Ge_2 belongs to the $I4/mmm$ space group, which has three mutually perpendicular mirror planes, giving rise to nodal lines in the absence of SOC (see Fig. S6(a)). However, the ferromagnetic magnetic ordering along [001] and the finite SOC break the mirror symmetry of $k_y=0$ and $k_x = 0$ mirror symmetry. Consequently, the degeneracy of the nodal lines is lifted as shown in Fig. S6(b). This leads to significant Berry curvature contributions along the nodal line, as shown in Fig. 5(c), which contribute directly to the intrinsic component of the AHC. The variation of the AHC with energy is shown in Fig. 5d. We found an intrinsic AHC (σ_{xy}^{int}) at E_F of about 100

$\Omega^{-1}cm^{-1}$ which is in excellent agreement with the pure intrinsic AHC observed in experiments in FM-1 phase. The structure at 0 K favors the magnetic ordering along [100] and we analyse this system with the same mirror symmetries. The electronic band structure is shown in Fig. 5e and we notice that the band crossing points have shifted 0.107 eV above E_F . These crossings remain intact in the presence of SOC and magnetic ordering along [100]. The red and blue lines represent the energy band in the presence and absence of SOC. The BC at E_F is shown in Fig. 5f and is negligible. The shift of these degenerate points above E_F leads to a lack of intrinsic AHC because there is no contribution from bands above E_F , which agrees with the experimental observations in FM-2 and FM-1 phase.

Discussion

To the best of our knowledge, this is the first report where one has shown that the nature of the AHE can be changed from completely intrinsic to extrinsic by changing the direction of the magnetic field from one crystallographic axis to another. This is even more noteworthy since in $SmMn_2Ge_2$, these two crystallographic axes [001] and [100] can both be magnetically easy axes depending on the temperature range one chooses. We have claimed the completely intrinsic AHE in FM-1 phase along c -axis based on the perfect linear fit between ρ_{yx}^A/M_s and ρ_{xx}^2 in Fig. 3(c). Although, this is enough for confirming intrinsic nature of AHE, one can also calculate the intrinsic contribution from the slope of the linear fit. Using the value of M_s at 150 K we get intrinsic component $\sigma_{xy}^{A(int)} = 107 \Omega^{-1}cm^{-1}$ demonstrating the absence of any extrinsic component. However, on applying magnetic field along a -axis, irrespective of whether we are in FM-1 (a -axis is the hard axis) or FM-2 (a -axis is the easy axis) we only observe extrinsic skew scattering dominated AHE. We have shown the σ_{Hall}^A against σ_{xx} for our $SmMn_2Ge_2$ along with other well-known AHE systems from the literature.^{5,7,21-28} It is clearly seen that σ_{Hall}^A monotonically increases as a function of σ_{xx} across FM-1 and FM-2

phases not depending on whether the magnetic field is aligned along the easy axis or hard axis. This is expected because the skew scattering mediated AHC depends only on the scattering time τ (or σ_{xx})^{22,29} provided M_s has no large fluctuation which is true for SmMn₂Ge₂ across FM-1 and FM-2. One can also define a skewness parameter ($S_{skew} = \frac{\sigma_{Hall}^A}{\sigma_{xx}}$) which only depends on the type of impurity.² Since the type of impurity is expected to be the same for SmMn₂Ge₂ across FM-1 and FM-2, we see a monotonic increase in σ_{Hall}^A with respect to σ_{xx} (shaded region in Fig. S7). The surprising result that at 2 K we observe only the normal Hall effect (see Fig. 4 (a)) in a ferromagnetic state with magnetic field along easy magnetic axis can be understood based on the how the normal Hall conductivity (σ_{xy}^N) and skew scattering mediated anomalous Hall conductivity ($\sigma_{xy}^{A,skew}$) depend on τ . Since the *RRR* of SmMn₂Ge₂ crystals are of the order of 10², the value of τ is very large at low temperature. σ_{xy}^N and $\sigma_{xy}^{A,skew}$ vary as τ^2 and τ , respectively. The value of τ at low temperature is expected to be large because the *RRR* of SmMn₂Ge₂ crystals are of the order of 10², hence, σ_{xy}^N dominates over $\sigma_{xy}^{A,skew}$ at low temperature.³⁰ As the temperature is increased, the value of τ decreases rapidly and therefore from 50 K onwards, we see clear signature of AHE.

Conclusion

We have investigated the anisotropic magneto-transport properties of SmMn₂Ge₂ which undergoes multiple magnetic phase transitions. In the high temperature ferromagnetic phase, we show that the observed anomalous Hall effect is completely intrinsic when the magnetic field is applied along the magnetic easy [001]. This can be completely tuned to a skew scattering mediated extrinsic anomalous Hall effect if the magnetic field direction is turned to magnetically hard *a*-axis. In the low temperature ferromagnetic phase, *a*-axis is magnetically easy axis, yet we do not observe an anomalous Hall effect at 2 K because the normal Hall effect easily dominates because of the large scattering time. Upon increasing the temperature, we

observe an extremely large anomalous Hall conductivity ($1400 \text{ } \Omega^{-1}\text{cm}^{-1}$) originating from skew scattering mechanism. In support to our experimental findings, the density functional theory-based calculations show that when the spins are aligned along [001], gapped nodal lines near the Fermi energy result in Berry curvature induced anomalous Hall conductivity of $\sim 100 \text{ } \Omega^{-1}\text{cm}^{-1}$. Upon aligning the spins along [100], these nodal line features shift above the Fermi energy that produces a negligible anomalous Hall conductivity.

Acknowledgement

NK acknowledges SERB for financial support through Grant Sanction No. CRG/2021/002747 and Max Planck Society for funding under Max Planck-India partner group project. This research project made use of the instrumentation facility provided by the Technical Research Centre (TRC) at the S. N. Bose National Centre for Basic Sciences, under the Department of Science and Technology, Government of India.

References

- 1 Xiao, D., Chang, M.-C. & Niu, Q. *Reviews of Modern Physics* **82**, 1959-2007, (2010).
- 2 Nagaosa, N., Sinova, J., Onoda, S., MacDonald, A. H. & Ong, N. P. *Reviews of Modern Physics* **82**, 1539-1592, (2010).
- 3 Nagaosa, N. & Tokura, Y. *Nature Nanotechnology* **8**, 899-911, (2013).
- 4 Manna, K. *et al. Physical Review X* **8**, 041045, (2018).
- 5 Nakatsuji, S., Kiyohara, N. & Higo, T. *Nature* **527**, 212-215, (2015).
- 6 Ye, L. *et al. Nature* **555**, 638-642, (2018).
- 7 Liu, E. *et al. Nature Physics* **14**, 1125-1131, (2018).
- 8 Guin, S. N. *et al. Advanced Materials* **33**, 2006301, (2021).
- 9 Fujii, H., Okamoto, T., Shigeoka, T. & Iwata, N. *Solid State Communications* **53**, 715-717, (1985).
- 10 Venturini, G., Welter, R., Ressouche, E. & Malaman, B. *Journal of Magnetism and Magnetic Materials* **150**, 197-212, (1995).
- 11 Barla, A., Sanchez, J. P., Malaman, B., Doyle, B. P. & Ruffer, R. *Physical Review B* **69**, 220405, (2004).
- 12 Gong, G. *et al. Physical Review Materials* **5**, 034405, (2021).
- 13 Zheng, X. *et al. Applied Physics Letters* **118**, (2021).
- 14 Perdew, J. P. & Wang, Y. *Physical Review B* **45**, 13244-13249, (1992).
- 15 Hafner, J. *Journal of Computational Chemistry* **29**, 2044-2078, (2008).
- 16 Pizzi, G. *et al. Journal of Physics: Condensed Matter* **32**, 165902, (2020).
- 17 Marzari, N. & Vanderbilt, D. *Physical Review B* **56**, 12847-12865, (1997).
- 18 Wu, Q., Zhang, S., Song, H.-F., Troyer, M. & Soluyanov, A. A. *Computer Physics Communications* **224**, 405-416, (2018).
- 19 Tian, Y., Ye, L. & Jin, X. *Physical Review Letters* **103**, 087206, (2009).
- 20 Zhang, G. *et al. Nature Communications* **13**, 5067, (2022).
- 21 Lee, M., Onose, Y., Tokura, Y. & Ong, N. P. *Physical Review B* **75**, 172403, (2007).
- 22 Shiomi, Y., Onose, Y. & Tokura, Y. *Physical Review B* **79**, 100404, (2009).
- 23 Miyasato, T. *et al. Physical Review Letters* **99**, 086602, (2007).
- 24 Iguchi, S., Hanasaki, N. & Tokura, Y. *Physical Review Letters* **99**, 077202, (2007).
- 25 Yang, S.-Y. *et al. Science Advances* **6**, eabb6003.
- 26 Fujishiro, Y. *et al. Nature Communications* **12**, 317, (2021).
- 27 Kanazawa, N. *et al. Physical Review Letters* **106**, 156603, (2011).
- 28 Takahashi, K. S. *et al. Science Advances* **4**, eaar7880.
- 29 Majumdar, A. K. & Berger, L. *Physical Review B* **7**, 4203-4220, (1973).
- 30 Schad, R., Beliën, P., Verbanck, G., Moshchalkov, V. V. & Bruynseraede, Y. *Journal of Physics: Condensed Matter* **10**, 6643, (1998).

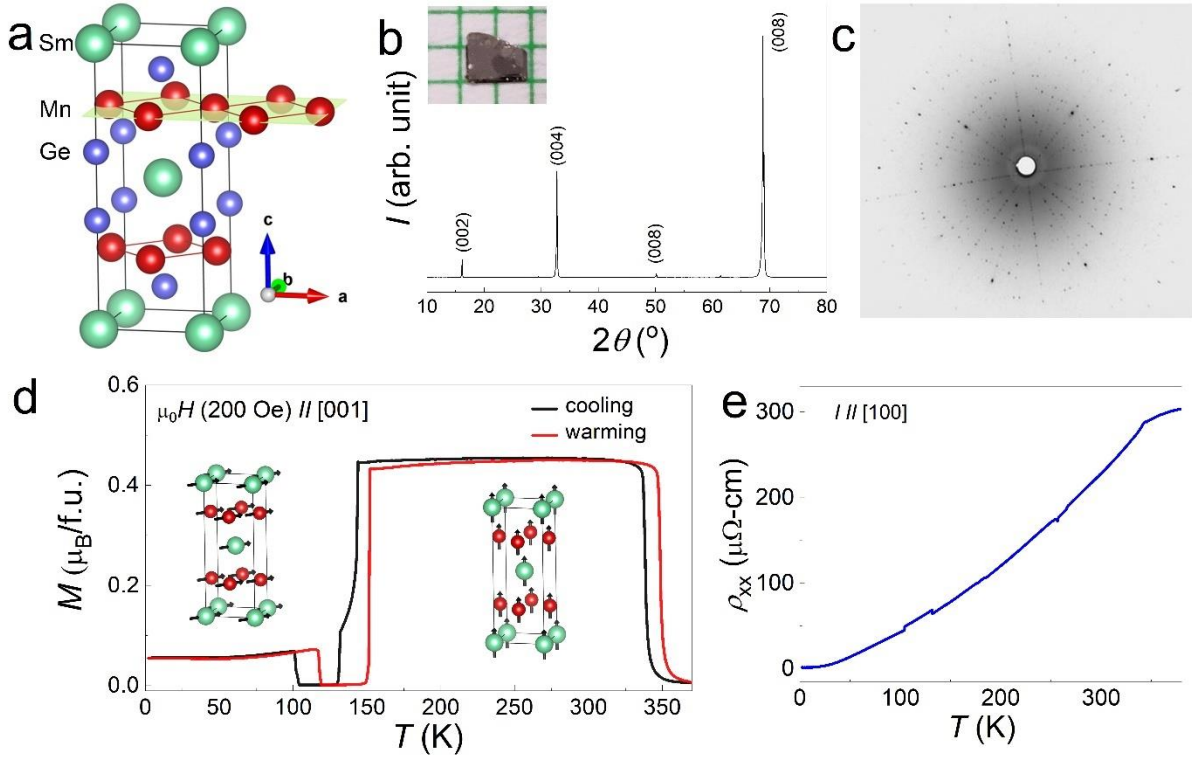


Fig. 1 (a) A unit cell of SmMn_2Ge_2 square net (highlighted by yellow plane) of Mn atoms, (b) x-ray diffraction pattern of SmMn_2Ge_2 single crystal with only ab-plane exposed to the x-ray. The diffraction pattern shows only (00l) reflections. The inset shows a typical single crystal placed on a graph paper. (c) The Laue diffraction pattern obtained by exposing the single crystal with the x-ray beam along [001]. (d) Magnetization versus temperature data obtained at a magnetic field of 200 Oe along [001] in the field cooled condition. Black and red lines show the data while cooling and warming, respectively. Spin alignments are shown for high temperature ferromagnetic region (FM-1) and low temperature ferromagnetic region (FM-2). (e) Longitudinal resistivity as a function of temperature in the absence of magnetic field by applying a current along [100].

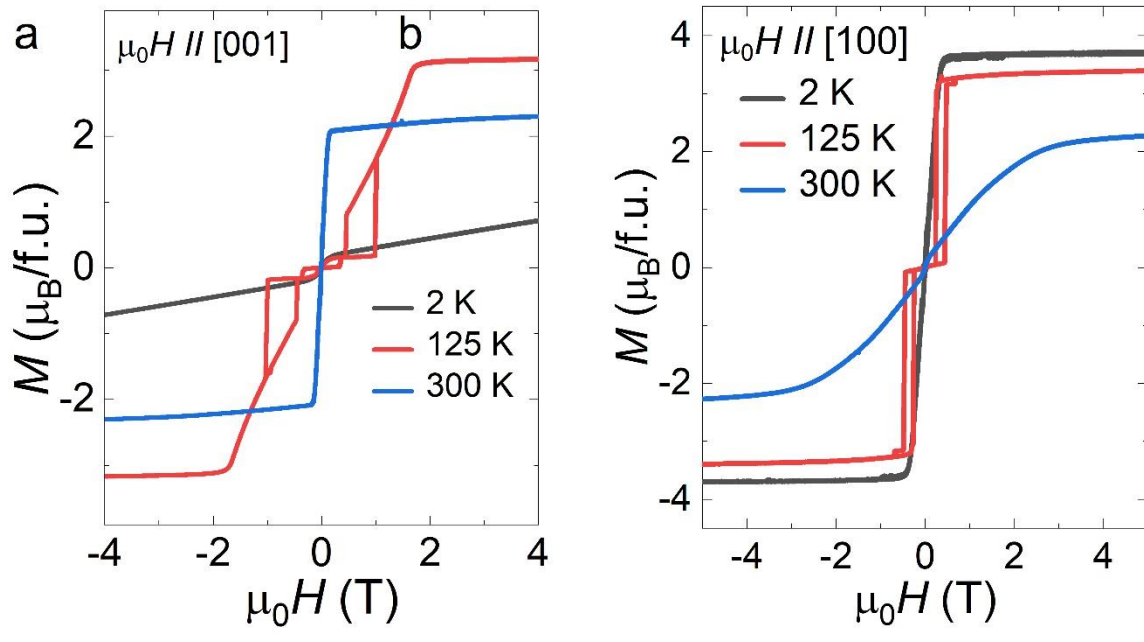


Fig. 2 Magnetization as a function of magnetic field at 2 K, 125 K and 300 K for applied magnetic field along (a) [001] and (b) [100].

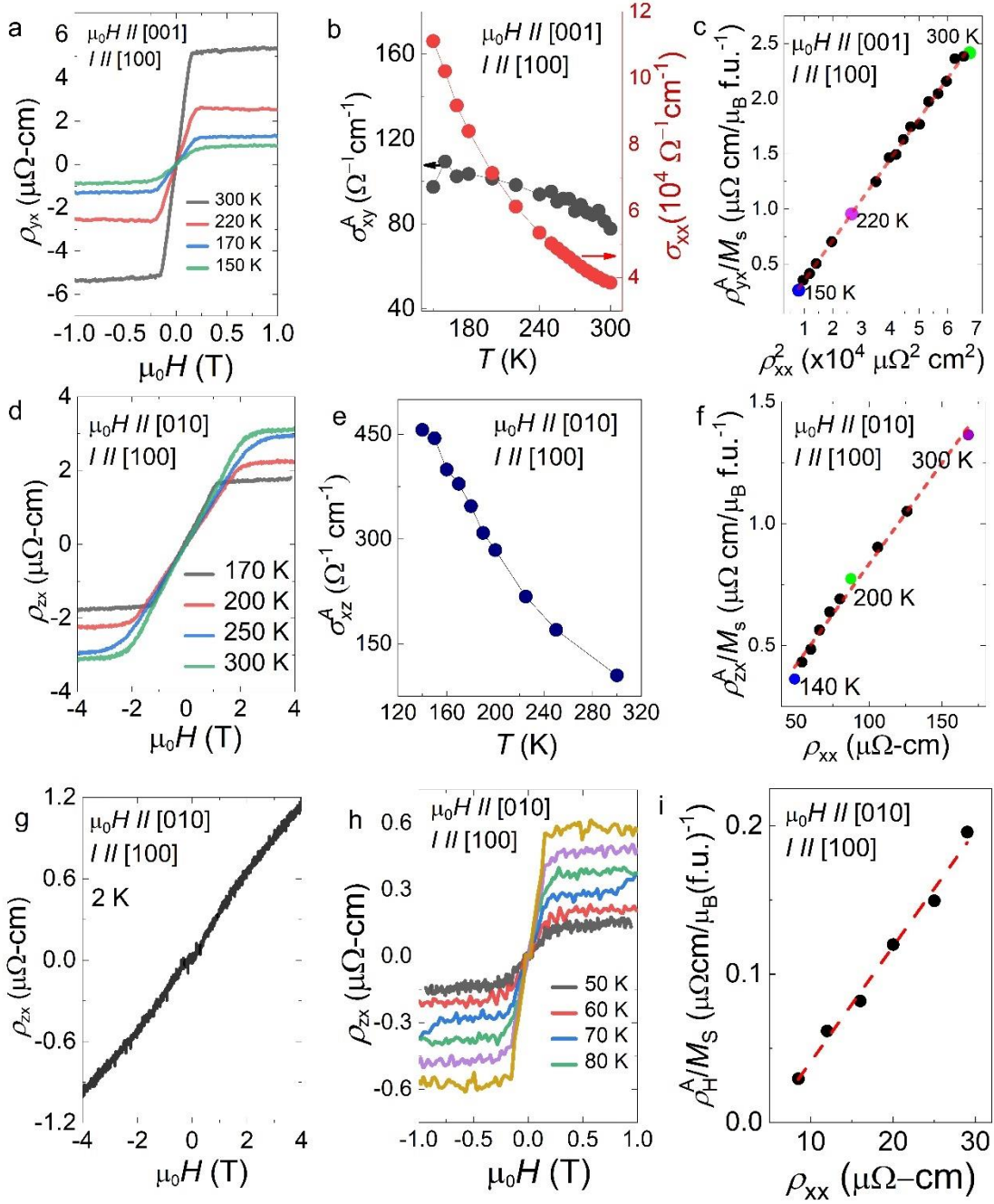


Fig. 3(a) ρ_{yx} versus $\mu_0 H$ data for $\mu_0 H$ along [001] at temperatures in FM-1 phase, (b) corresponding σ_{xy}^A (left-axis) and σ_{xx} (right-axis) with temperature in FM-1 phase, (c) ρ_{yx}^A/M_s versus ρ_{xx}^2 for $\mu_0 H$ along [001] in FM-1 phase. (d) ρ_{zx} versus $\mu_0 H$ data for $\mu_0 H$ along [010] at temperatures in FM-1 phase, (e) corresponding σ_{xz}^A with temperature in FM-1 phase, (f) ρ_{zx}^A/M_s versus ρ_{xx} for $\mu_0 H$ along [010] in FM-1 phase. (g) ρ_{zx} versus $\mu_0 H$ data for $\mu_0 H$ along [010] at 2 K in FM-2 phase, (h) ρ_{zx} versus $\mu_0 H$ data for $\mu_0 H$ along [010] at from 50 to 80 K in FM-2 phase, (i) ρ_{yx}^A/M_s versus ρ_{xx} for $\mu_0 H$ along [010] in FM-2 phase.

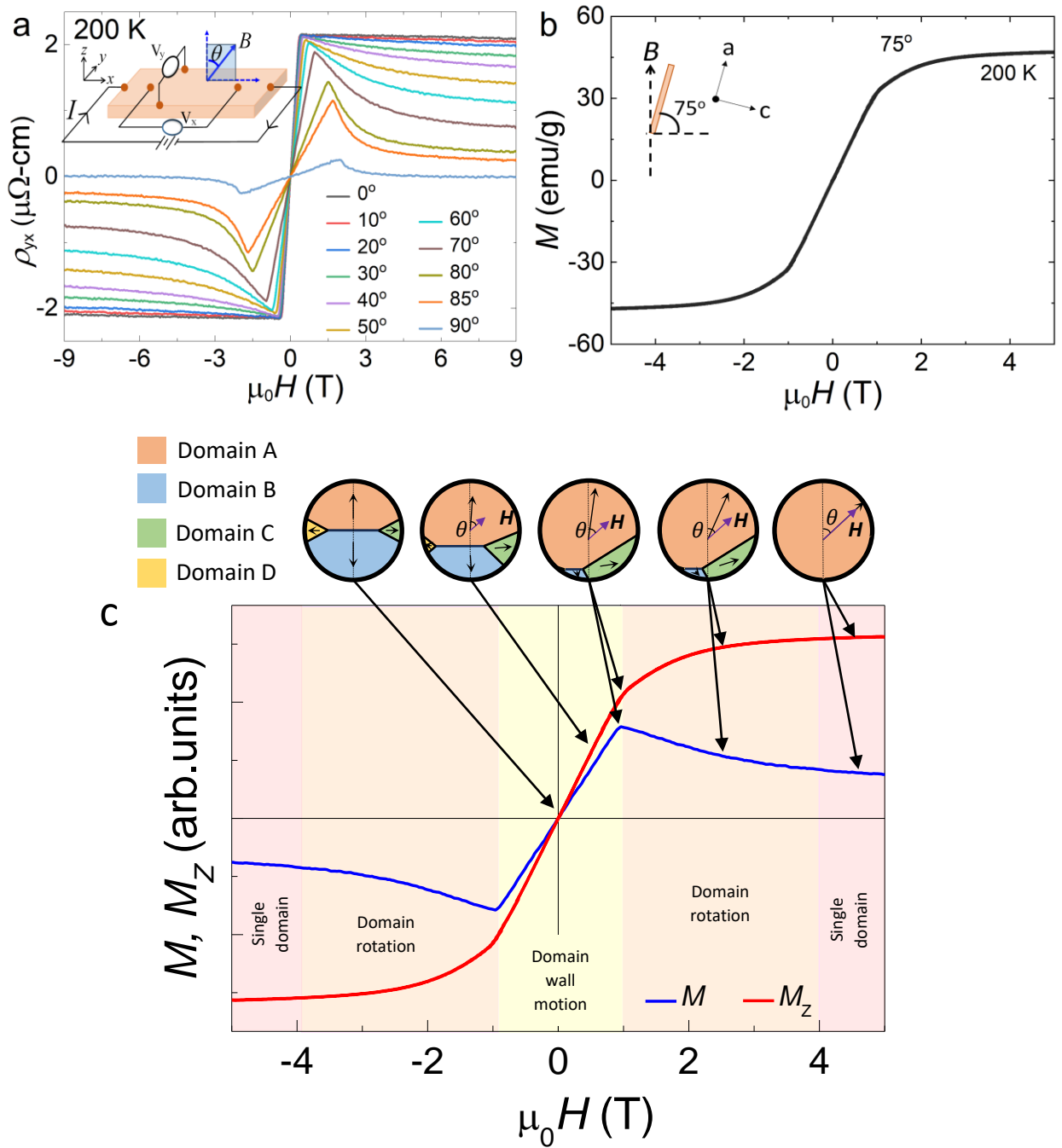


Fig. 4(a) ρ_{yx} versus $\mu_0 H$ data at 200 K at different angles with $\theta = 0^\circ$ and 90° corresponding to $\mu_0 H$ along [001] and [100], respectively, (b) corresponding M versus H data at $\theta = 75^\circ$. (c) Net magnetisation (M) and the z-component of the net magnetisation (M_z) as the function of magnetic field applied at an angle θ away from the c -axis as explained by the possible domain evolution.

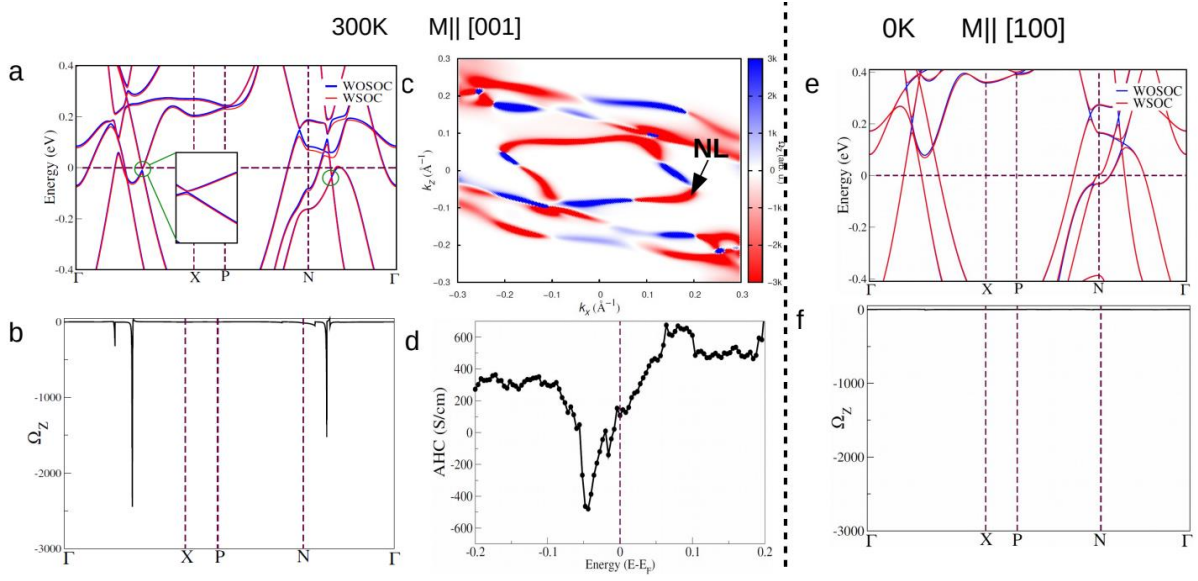


Fig. 5(a) The band structure of SmMn_2Ge_2 without SOC and with SOC at 300 K where the spins are oriented along $[001]$. The gapped nodal lines are shown in the inset. (b) The z -component of Berry curvature peaks along the high-symmetry lines due to the gapped nodal lines. (c) Along the gapped nodal line, the Berry curvature distribution is shown at $k_y = 0$ plane (d) Energy ($E - E_F$) dependence of the AHC for SmMn_2Ge_2 . (e) The band structure of SmMn_2Ge_2 without SOC and with SOC at 0 K. (f) The z -component of Berry curvature along the high symmetry lines.